杨海翔 列第一，排名第二

Energy & Environmental Science

ROYAL SOCIETY OF CHEMISTRY

PAPER

View Article Online
View Journal | View Issue

Cite this: *Energy Environ. Sci.*, 2025, 18, 5470

Tetragonal ZrO_2 supported low-iridium catalyst activating oxygen spillover stabilized lattice oxygen for proton exchange membrane water electrolysis†

Song Ru Fang,‡[a] Hai Xiang Yang,‡[a] Hao Yang Lin,[a] Miao Yu Lin,[a] Fang Xin Mao,[a] Hao Fan,[a] Huai Qin Fu,[b] Hai Yang Yuan, *[a] Chenghua Sun, [c] Peng Fei Liu *[a] and Hua Gui Yang *[a]

Mediating the trade-off between activity and durability at a low Ir loading is challenging for the acidic oxygen evolution reaction (OER) in proton exchange membrane (PEM) water electrolysis. Herein, we construct an efficient and stable low-iridium loaded anode electrocatalyst supported on porous tetragonal zirconium oxide (IrO_x/t-ZrO_2) that exhibits a high mass activity of 1464.6 A g_{Ir}^{-1} at 1.6 V and can operate stably at 10 mA cm^{-2} for more than 1000 h in acidic electrolyte without any degradation. Structural characterization studies, electrochemical analyses and theoretical calculations reveal active lattice oxygen redox over a supported IrO_x nanocluster, stabilized by oxygen spillover from the t-ZrO_2 substrate during the OER process. This oxygen spillover engaged lattice oxygen oxidation pathway can not only boast OER kinetics *via* avoiding scaling relationships between oxygen intermediates, but also prevent the collapse of IrO_x by the prompt recovery of migrated oxygen species. A PEM electrolyzer using IrO_x/t-ZrO_2 as the anode material, with a significantly low Ir loading of 0.1 mg_{Ir} cm^{-2}, demonstrates 3.10 A cm^{-2} at only 1.9 V, and low activity decay (6.25 μV h^{-1}) during a 1600 h test at 1 A cm^{-2}.

Received 27th January 2025,
Accepted 11th April 2025

DOI: 10.1039/d5ee00544b

rsc.li/ees

Broader context

Proton exchange membrane water electrolysis (PEMWE) plays an important role in converting renewable energy into green hydrogen. However, the scalable development of PEMWE is hindered by the consumption of Ir. Therefore, improving the activity and stability of Ir-based catalysts is imperative to decrease the loading level of Ir. Here, we report a tetragonal ZrO_2 supported low-iridium catalyst fabricated *via* a molten salt method. This configuration activates the kinetically favored lattice oxygen oxidation mechanism pathway and can trigger the spillover from t-ZrO_2 to Ir sites to prevent the collapse of the catalyst structure. Benefiting from the unique oxygen diffusion between support and active sites, we have constructed a PEM electrolyzer with high activity and long-term stability at a low Ir loading amount (0.1 mg_{Ir} cm^{-2}).

Introduction

Proton exchange membrane (PEM) water electrolysis offers advantages of high operating current density, high hydrogen purity, rapid response and compact design, rendering it one of the most promising technologies to convert renewable energy into green hydrogen.[1,2] To date, only iridium (Ir)-based materials as the benchmark commercial electrocatalysts for the oxygen evolution reaction (OER) have been utilized in practical PEM water electrolysis on account of their extraordinary stability.[3–5] Unfortunately, high loading amounts of Ir (2–4 mg cm^{-2}) as anodic catalysts are required for traditional commercial PEM electrolyzers to meet the demands in industrial applications,[1,3,6] and the low earth abundance and high cost of Ir significantly hinder the further deployment of this technology to a great extent. Although in recent research studies the stability and activity of Ir-based catalysts are improved to a great degree, a loading of 0.5–2 mg_{Ir} cm^{-2} remains necessary for these supported catalysts to exhibit satisfactory activity and stability in PEM

[a] *Key Laboratory for Ultrafine Materials of Ministry of Education, School of Materials Science and Engineering, East China University of Science and Technology, Shanghai 200237, China. E-mail: pfliu@ecust.edu.cn, hyyuan@ecust.edu.cn, hgyang@ecust.edu.cn*

[b] *Centre for Catalysis and Clean Energy, Gold Coast Campus, Griffith University, Gold Coast, QLD 4222, Australia*

[c] *Department of Chemistry and Biotechnology, and Center for Translational Atomaterials, Swinburne University of Technology, Hawthorn, VIC, 3122, Australia*

† Electronic supplementary information (ESI) available. See DOI: https://doi.org/10.1039/d5ee00544b

‡ These authors contributed equally.

electrolyzers.[7–9] Therefore, it is still challenging to reduce the loading amount down to 0.5 mg_{Ir} cm^{-2} while maintaining the activity and stability for large-scale implementation of PEM water electrolysis.

Previous studies have focused on enhancing the intrinsic activity of Ir-based materials to reduce the loading amounts. To achieve this goal, great breakthroughs have been achieved in low-iridium PEM electrolyzers in academia, such as introducing fine grain boundaries into the torsion-strained $Ta_{0.1}Tm_{0.1}Ir_{0.8}O_{2-\delta}$,[10] constructing short-range ordered $IrO_x \cdot H_2O$ with lattice water-assisted oxygen exchange,[7] and atomically dispersing hexavalent iridium oxide (Ir_{VI}-ado)[3] into the oxidative MnO_2 matrix. For comparison, supported Ir-based anode electrocatalysts have already been successfully applied in commercial PEM electrolyzers, utilizing acid-stable metal oxide with a wide electrochemical window as the support.[11] For example, commercial anode electrocatalysts such as an Elyst Ir75 0480[12] (Umicore, with 75 wt% Ir content) and a P2X[13] (Heraeus, with 45 wt% Ir content) were constructed by dispersing active Ir species onto the TiO_2 supports, thereby reducing the Ir loading amount. Furthermore, recent research studies have explored diverse supports to construct efficient support interfaces,[14,15] and to achieve high electrical conductivity (*e.g.*, TaB,[16] Zr_2ON_2,[17] TiN[18] *etc.*) and hierarchical nanostructures,[19,20] leading to the improved performance in PEM electrolyzers. Unfortunately, a loading of 0.5–2 mg_{Ir} cm^{-2} is necessary for these supported catalysts to exhibit satisfactory activity and stability in PEM electrolyzers. Consequently, there is an urgent need to develop novel supported catalysts that can achieve comparable performance with reduced Ir loading.

Tuning the OER pathways can effectively mediate the trade-off between activity and stability,[21,22] which has been successfully implemented in supported Ir-based electrocatalysts for acidic water oxidation.[8,23,24] The kinetically preferred lattice oxygen oxidation mechanism (LOM) can directly form $*OO^{2-}$ without *OOH formation, which is the intermediate of the adsorbate evolution mechanism (AEM), thus breaking the scaling relationships between oxygen-containing intermediates and reducing overpotentials.[25] However, the participation of lattice oxygen will also generate dissolvable high-valence metal oxides, resulting in the collapse of the catalyst structures with poor stability.[26,27] In this regard, most developed OER electrocatalysts have been modulated to follow the AEM pathway totolerate the harsh environment in PEM electrolyzers,[28–30] which would inevitably sacrifice the activity. Recently, oxygen spillover has been proposed to improve the activity, selectivity and stability in heterogeneous catalysis such as CO oxidation[31–33] and various CO_2 hydrogenation reactions.[34] However, in electrochemistry especially oxygen electrocatalysis, the oxygen spillover mechanism was subtly manipulated to avoid the overoxidation of the catalytic sites[8,35] or support sites,[36] accompanied by oxygen migration from the unstable sites; conversely, for the supported Ir-based electrocatalysts, we anticipate that prompt recovery of lattice oxygen into the unstable IrO_x configurations would synergistically enhance the activity and stability when activating the LOM pathway.

Among the metal oxide substrates, ZrO_2 particles have recently been widely studied due to their hydrophilicity, thermo-mechanical strength, chemical stability and hydroxide ion transport ability in the fabrication of anion exchange membranes,[37,38] and these properties make ZrO_2 suitable as a support for OER catalysts. In this article, a low-iridium loaded anode electrocatalyst supported on porous tetragonal zirconium oxide (IrO_x/t-ZrO_2) has been successfully constructed for efficient and durable acidic water oxidation. Our structural characterization studies, electrochemical analyses and theoretical calculations reveal active lattice oxygen redox over a supported IrO_x nanocluster, stabilized by oxygen spillover from t-ZrO_2 supports during the OER process. The resultant IrO_x/t-ZrO_2 catalyst can be applied in a PEM electrolyzer as the anode material, with an extremely low Ir loading of 0.1 mg_{Ir} cm^{-2}, which achieves a current density of 3.10 A cm^{-2} at a cell voltage of 1.9 V, and continuously operates over 1600 h at 1 A cm^{-2} with low activity decay (6.25 μV h^{-1}). Thus, our t-ZrO_2 supported catalyst can allow the Ir loading amount to be reduced by >95% compared with the present level (2 to 4 mg_{Ir} cm^{-2}) without compromising the activity or stability.

Results and discussion

Reaction mechanism designs and theoretical studies

The Fig. S1a and b (ESI†) illustrate the traditional AEM and LOM pathways during the OER process, respectively. The AEM pathway involves four concerted proton–electron transfer steps, which lead to a scale relationship between the binding energies of *OH and *OOH. In contrast, the LOM pathway involves non-concerted proton–electron transfer steps and the formation of energetically favorable O–O couples by engaging lattice oxygen, thus bypassing the formation of *OOH seen in the AEM pathway. However, as shown in Fig. 1a, excessive participation of lattice oxygen in the LOM pathway can also form soluble $*V_O$–IrO_4^{2-} intermediates and result in catalyst collapse.[26,39]

Here we propose an oxygen spillover stabilized LOM pathway and anticipate that the high-valence Ir sites could be stabilized by introducing a support capable of readily absorbing oxygen from water dissociation and facilitating its spillover to recover the active lattice oxygen sites (Fig. 1a and Fig. S1c, ESI†). Among the acid-stable metal oxides as substrates,[11] strategies have been implemented to balance the activity and stability for the supported electrocatalysts: using WO_x[40,41] as Brønsted acid sites to motivate the deprotonation of surface OH, Nb_2O_5[8] and MoO_3[35] as acceptors of oxygen species to inherit the overoxidation of the active sites, SnO_2[24] with an excess electron reservoir as an electron donator to promote the charge transfer. Nevertheless, in none of the above could the metal oxides as a support dissociate H_2O to generate sufficient oxygen species and thus supply the consumed lattice oxygen through oxygen spillover. Zirconia (ZrO_2) ceramic typically featured with excellent corrosion resistance, also shows a strong electrochemical oxidation resistance,

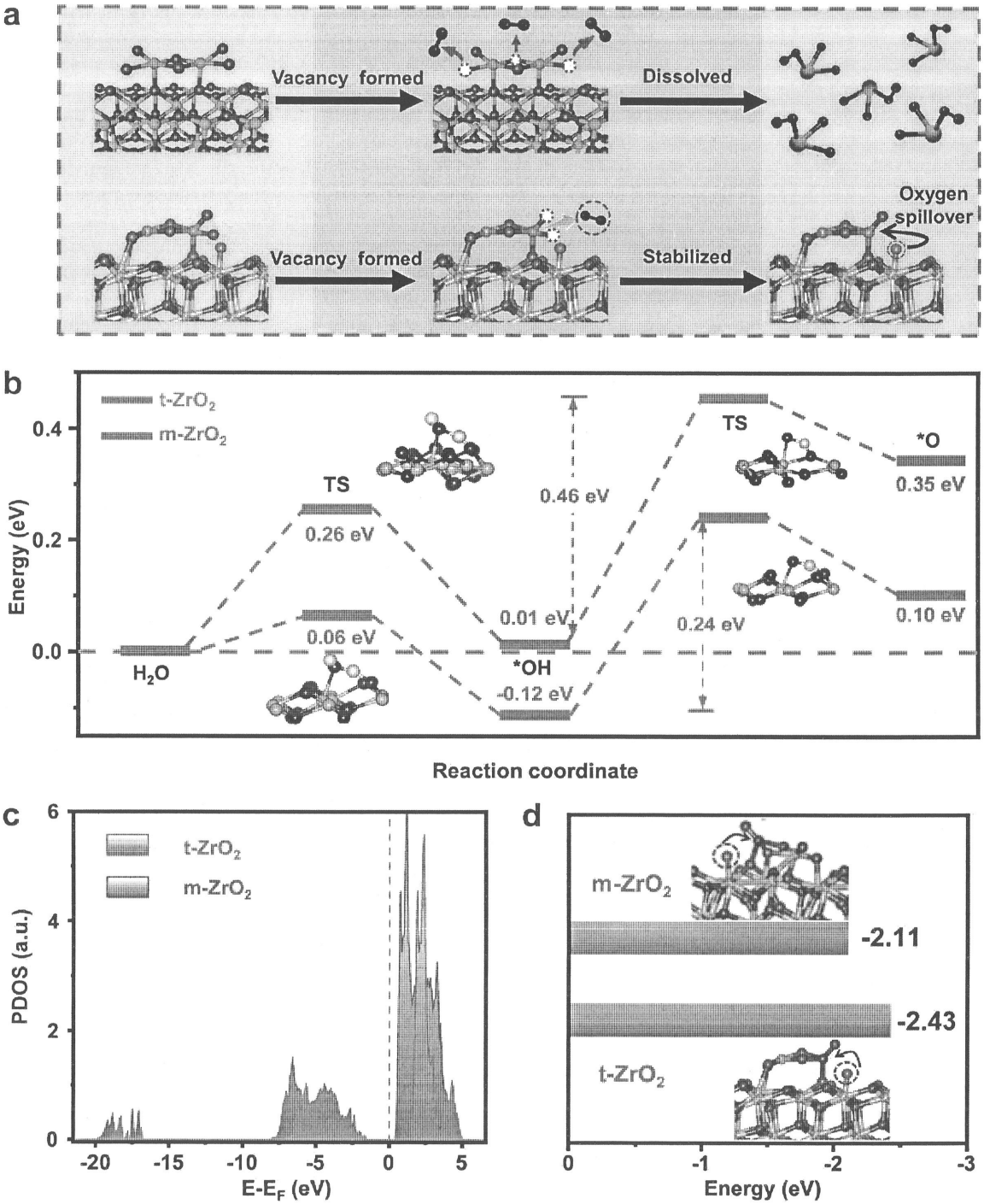

Fig. 1 The illustration of the oxygen spillover stabilized LOM pathway and DFT calculation. (a) Scheme of the dissolution of catalyst in the LOM pathway (up) and oxygen spillover stabilized LOM pathway on the IrO_x/t-ZrO_2 catalyst (down). (b) Free energy changes of water dissociation in t-ZrO_2 and m-ZrO_2 supports. (c) Projected density of state (PDOS) of the d orbital of Zr of t-ZrO_2 and m-ZrO_2. (d) The energy of oxygen diffusion on IrO_x/t-ZrO_2 and IrO_x/m-ZrO_2. The inset shows the scheme of oxygen diffusion on IrO_x/t-ZrO_2 (left) and IrO_x/m-ZrO_2 (right).

which makes it suitable as an anode support for PEM electrolyzers; previous studies have demonstrated that different from the most stable monoclinic phase (m-ZrO_2), the tetragonal phase of ZrO_2 (t-ZrO_2) allows for thermodynamically accessible oxygen spillover from Zr sites to the other interacted metal sites.[42,43]

Based on the above discussions, density functional theory (DFT) calculations were conducted to study the possibility of

the oxygen spillover from Zr to Ir sites with different phases of ZrO_2. As shown in Fig. S2 (ESI†), the Zr^{4+} site on the surface is bonded in a distorted body-centered cubic geometry to seven equivalent O^{2-} atoms in t-ZrO_2; for m-ZrO_2, the Zr^{4+} site on the surface is bonded to six O^{2-} atoms to form a mixture of distorted corner and edge-sharing ZrO_6 pentagonal bipyramids. The different configurations of the O-coordinated Zr site may lead to different water dissociation abilities for different phases of t-ZrO_2 and m-ZrO_2. As shown in Fig. 1b, the H_2O dissociation into O species on t-ZrO_2 has energy barriers of only 0.06 and 0.10 eV, which are about 0.20 and 0.25 eV lower than that that on m-ZrO_2. This result illustrates that t-ZrO_2 exhibits greater reactivity compared to m-ZrO_2 for the H_2O dissociation into O. To further understand the superior H_2O dissociation of t-ZrO_2, we made quantitative analyses on the projected density of states (PDOS) of on m-ZrO_2 and t-ZrO_2. As illustrated in Fig. 1c the d-band center (−6.03 eV) for the Zr site on t-ZrO_2 is situated in closer proximity to the Fermi energy (E_F) in comparison to m-ZrO_2 (−6.15 eV). This proximity to the Fermi energy endows t-ZrO_2 with enhanced activation capability for H_2O, thus leading to lower energy barrier of the H_2O dissociation on t-ZrO_2. Besides, we have further explored H_2O dissociation on IrO_x-loaded systems (IrO_x/m-ZrO_2 and IrO_x/t-ZrO_2). As shown in Fig. S3 (ESI†), it can be found that the H_2O dissociation barriers on IrO_x/t-ZrO_2 exhibit remarkably low barriers of 0.07 eV and 0.17 eV, respectively; while, on IrO_x/m-ZrO_2, the corresponding barriers for H_2O dissociation are 0.38 eV and 1.54 eV, which are much higher than those on IrO_x/t-ZrO_2. This demonstrates that t-ZrO_2 maintains its intrinsic water dissociation superiority over m-ZrO_2 even after IrO_x deposition.

Additionally, we explored the oxygen diffusion energies from ZrO_2 to IrO_x, as shown in Fig. 1d, the energy for diffusion from Zr sites on t-ZrO_2 to the supported IrO_x is more negative (−2.43 eV), implying that the oxygen diffusion on IrO_x/t-ZrO_2 could be feasible and easier, thus better providing the oxygen species for the OER on IrO_x and stabilizing the Ir sites. This theoretical result illustrates that the oxygen spillover stabilized LOM pathway mechanism could be favored, where the oxygen species can promptly replenish the lost lattice oxygen, avoiding the dissolution of IrO_x.

Synthesis and structural characterization of the IrO_x/t-ZrO_2 catalyst

Inspired by the above theoretical results, we rationally constructed catalysts with highly dispersed IrO_x loaded in different phases of ZrO_2 (IrO_x/t-ZrO_2 and IrO_x/m-ZrO_2) using a molten salt method. Initially, UIO-66 was synthesized *via* a solvothermal method, and the scanning electron microscopy (SEM) images (Fig. S4a and b, ESI†) reveal its octahedral architecture. It was also characterized using X-ray diffraction (XRD) where its diffraction peaks match simulated patterns well (Fig. S5, ESI†). Subsequently, Ir precursors were absorbed onto the framework of the UIO-66 under vigorous stirring, resulting in the formation of Ir@UIO-66. A homogeneous mixture of Ir@UIO-66 and salts (60% $NaNO_3$ + 40% KNO_3) was then obtained through rotary evaporation to obtain dry salts. Eventually, IrO_x/t-ZrO_2 was further constructed after calcining the mixture at 450 °C in molten salt (Fig. 2a, see Methods for more details). The XRD pattern (Fig. 2b) of IrO_x/t-ZrO_2 exhibits similar crystal structures to t-ZrO_2 with major peaks of t-ZrO_2 (PDF#97-009-7004). After loading Ir, the diffraction peaks at 34.8° show higher intensities and can be allocated to the (101) plane of IrO_2 (PDF#97-064-0887), while the XRD pattern (Fig. S6, ESI†) of IrO_x/m-ZrO_2 exhibit similar crystal structures to m-ZrO_2, except for the broadened peak at ~35° which refers to the (101) plane of IrO_2. The Ir content was confirmed using inductively coupled plasma optical emission spectroscopy (ICP-OES), revealing Ir loadings of ~20 wt% (20 mg Ir in 100 mg catalyst) for sample IrO_x/t-ZrO_2 and ~24 wt% (24 mg Ir in 100 mg catalyst) for sample IrO_x/m-ZrO_2.

Brunauer–Emmett–Teller (BET) adsorption–desorption isotherm (Fig. 2c and Fig. S7, ESI†) reveals that the precursor UIO-66 has a surface area of 1158.46 $m^2\ g^{-1}$, and after the molten salt procedure, the as synthesized IrO_x/t-ZrO_2 catalyst still retains a high surface area of 187.71 $m^2\ g^{-1}$ which is significantly higher than that of IrO_x/m-ZrO_2 (53.44 $m^2\ g^{-1}$). As shown in the transmission electron microscopy (TEM) images (Fig. 2d and Fig. S8a and b, ESI†), IrO_x clusters (~1.34 nm) are densely loaded on porous ZrO_2 in IrO_x/t-ZrO_2. In order to further investigate the atomic status of IrO_x in the IrO_x/t-ZrO_2 catalyst, aberration-corrected high-angle annular dark-field scanning TEM (HAADF-STEM) was utilized. It can be demonstrated that IrO_x clusters, inferred using the Z contrast analysis, are loaded onto the (101) plane of t-ZrO_2 (Fig. 2e and Fig. S9a and b, ESI†). Moreover, the corresponding energy dispersive spectrometer (EDS) elemental mappings using HAADF-STEM (Fig. 2f) can further confirm that IrO_x clusters are well dispersed on ZrO_2. Similarly, it is confirmed that the IrO_x clusters (~1.46 nm) of IrO_x/m-ZrO_2 are evenly distributed on m-ZrO_2, characterized by TEM, HAADF-STEM images and corresponding EDS elemental mappings (Fig. S10a–e, S11a and b, ESI†).

Evaluation of acidic water oxidation performance

To evaluate the electrochemical OER performance of IrO_x/t-ZrO_2, a three-electrode electrochemical system was utilized in N_2-saturated 0.1 M $HClO_4$ electrolyte, with IrO_x/m-ZrO_2 commercial Ir black (catalyst grade) and commercial IrO_2 (catalyst grade) serving as reference samples, and the potentials in all tests were normalized to the reversible hydrogen electrode (RHE) with the calibrated Ag/AgCl (3.5 M KCl) reference electrode (Fig. S12, ESI†). Linear sweep voltammetry (LSV) was performed to assess the overpotential of the catalysts (Fig. 3a). We firstly compared the OER activity with different Ir contents (Fig. S13, ESI†); as the Ir content increased (from 20 wt% to 50 wt%), the electrocatalytic activity increased slightly. For the consideration of atomic usage of Ir, the catalyst with a loading of 20 wt% is selected for illustration. IrO_x/t-ZrO_2 exhibited the lowest overpotential at 10 mA cm^{-2} (287.5 mV), outperforming IrO_x/m-ZrO_2 (324.4 mV), commercial Ir black (330.1 mV) and commercial IrO_2 (343 mV). Considering the loading of Ir as a crucial indicator of the catalyst's practi-

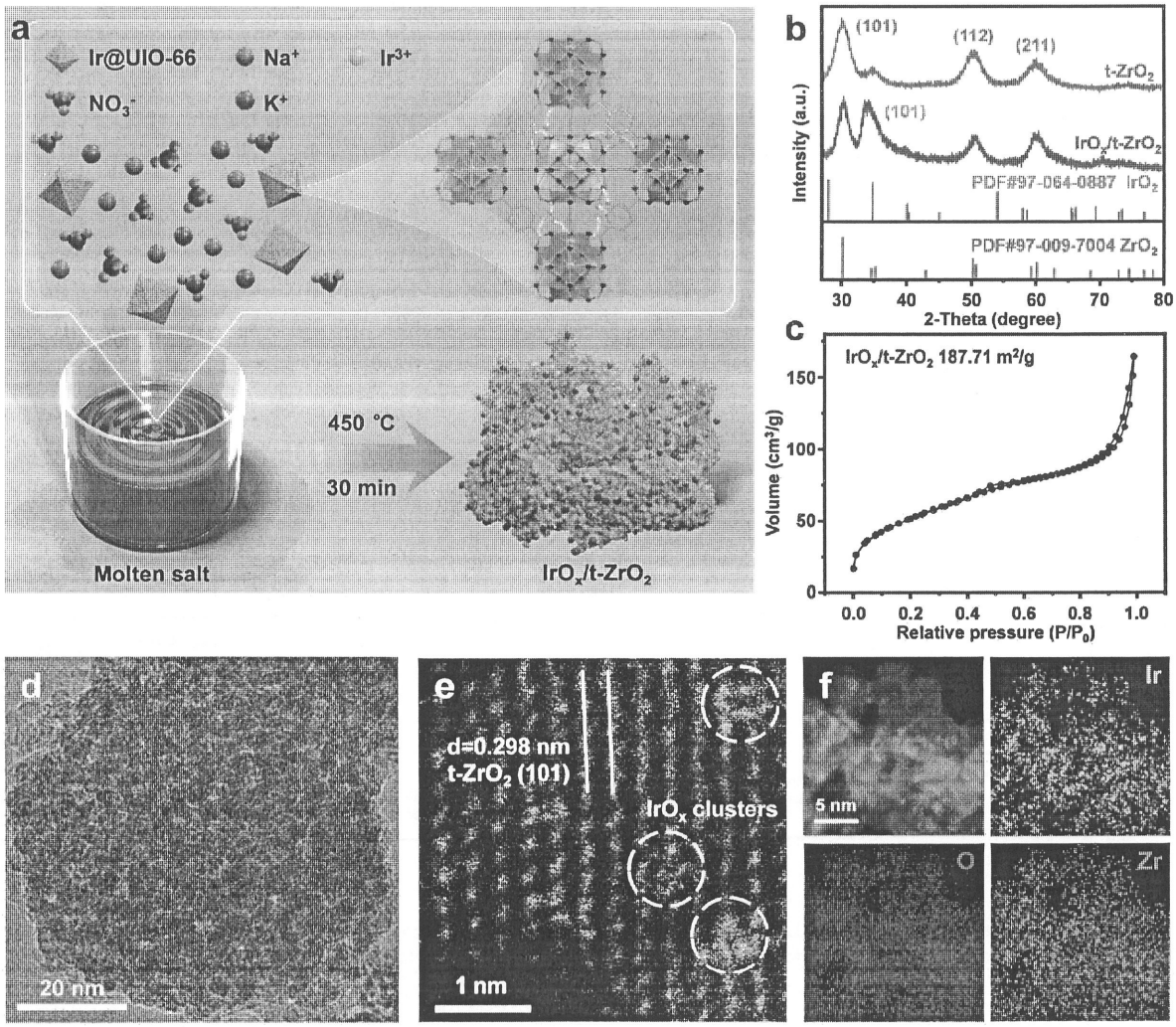

Fig. 2 The synthetic strategy schematic and structural characterization of the $IrO_x/t\text{-}ZrO_2$ electrocatalyst. (a) Scheme of the preparation of the $IrO_x/t\text{-}ZrO_2$ electrocatalyst. (b) XRD patterns of $t\text{-}ZrO_2$ and $IrO_x/t\text{-}ZrO_2$. The PDF cards of $t\text{-}ZrO_2$ (PDF#97-009-7004) and IrO_2 (PDF#97-064-0887) are marked green and orange, respectively. (c) BET adsorption–desorption isotherm of $IrO_x/t\text{-}ZrO_2$. (d) TEM images of as-synthesized $IrO_x/t\text{-}ZrO_2$. (e) Atomic-resolution aberration-corrected HAADF-STEM image of $IrO_x/t\text{-}ZrO_2$ in which the bright spots highlighted by the circles are ascribed to IrO_x clusters and a lattice distance of 0.298 nm are ascribed to the (101) plane of $t\text{-}ZrO_2$. (f) HAADF-STEM image of $IrO_x/t\text{-}ZrO_2$ and corresponding elemental maps of Ir, Zr and O, showing the homogenous dispersion within the catalyst.

cality, mass activity was also evaluated (Fig. 3b). The mass activity of $IrO_x/t\text{-}ZrO_2$ was determined to be 609.1 A g_{Ir}^{-1} and 1457.4 A g_{Ir}^{-1} at 1.55 V and 1.60 V, respectively, surpassing $IrO_x/m\text{-}ZrO_2$ (206.9 A g_{Ir}^{-1} and 601.4 A g_{Ir}^{-1}, respectively), commercial Ir black (46.7 A g_{Ir}^{-1} and 110.7 A g_{Ir}^{-1}, respectively) and commercial IrO_2 (45.0 A g_{Ir}^{-1} and 160.45 A g_{Ir}^{-1}, respectively), shown in Fig. 3c. In addition, $IrO_x/t\text{-}ZrO_2$ demonstrated a lower Tafel slope of 51.5 mV dec^{-1} compared to $IrO_x/m\text{-}ZrO_2$ (71.6 mV dec^{-1}), shown in Fig. 3d, which matches well with the electrochemical impedance spectroscopy (EIS). The obtained EIS results were fitted based on the equivalent circuit,[44] where $IrO_x/t\text{-}ZrO_2$ shows a smaller semicircle representing the lower charge transfer resistance (R_{ct} = 3.76 Ω cm^2) compared to $IrO_x/m\text{-}ZrO_2$ (R_{ct} = 7.31 Ω cm^2) (Fig. 3e), reflecting the faster kinetic rate of $IrO_x/t\text{-}ZrO_2$. Furthermore, benefiting from its large BET surface, the $IrO_x/t\text{-}ZrO_2$ also showed a superior electrochemical active surface area (ECSA) of 845 cm_{oxide}^{-2} compared to $IrO_x/m\text{-}ZrO_2$ (594 cm_{oxide}^{-2}) (Fig. S14a, b and S15a, b, ESI†). The ECSA normalized specific activity shown in Fig. 3f also indicates that the intrinsic activity of $IrO_x/t\text{-}ZrO_2$ is better than $IrO_x/m\text{-}ZrO_2$.

To further study the durability of the catalyst, a long-term chronopotentiometric (CP) test was carried out using 1 cm^2 carbon paper (catalyst loading: 1 mg cm^{-2}, 0.2 mg_{Ir} cm^{-2}). As shown in Fig. 3g, only 1.5 V was required for $IrO_x/t\text{-}ZrO_2$ to reach a current density of 10 mA cm^{-2}, and maintains a high activity with a negligible degradation rate after 1000 h test. The dissolution rate of the catalyst is also crucial for assessing catalyst stability. Hence, inductively coupled plasma mass spectrometry (ICP-MS) was conducted to measure the catalyst's dissolution rate during the stability test. The results indicate

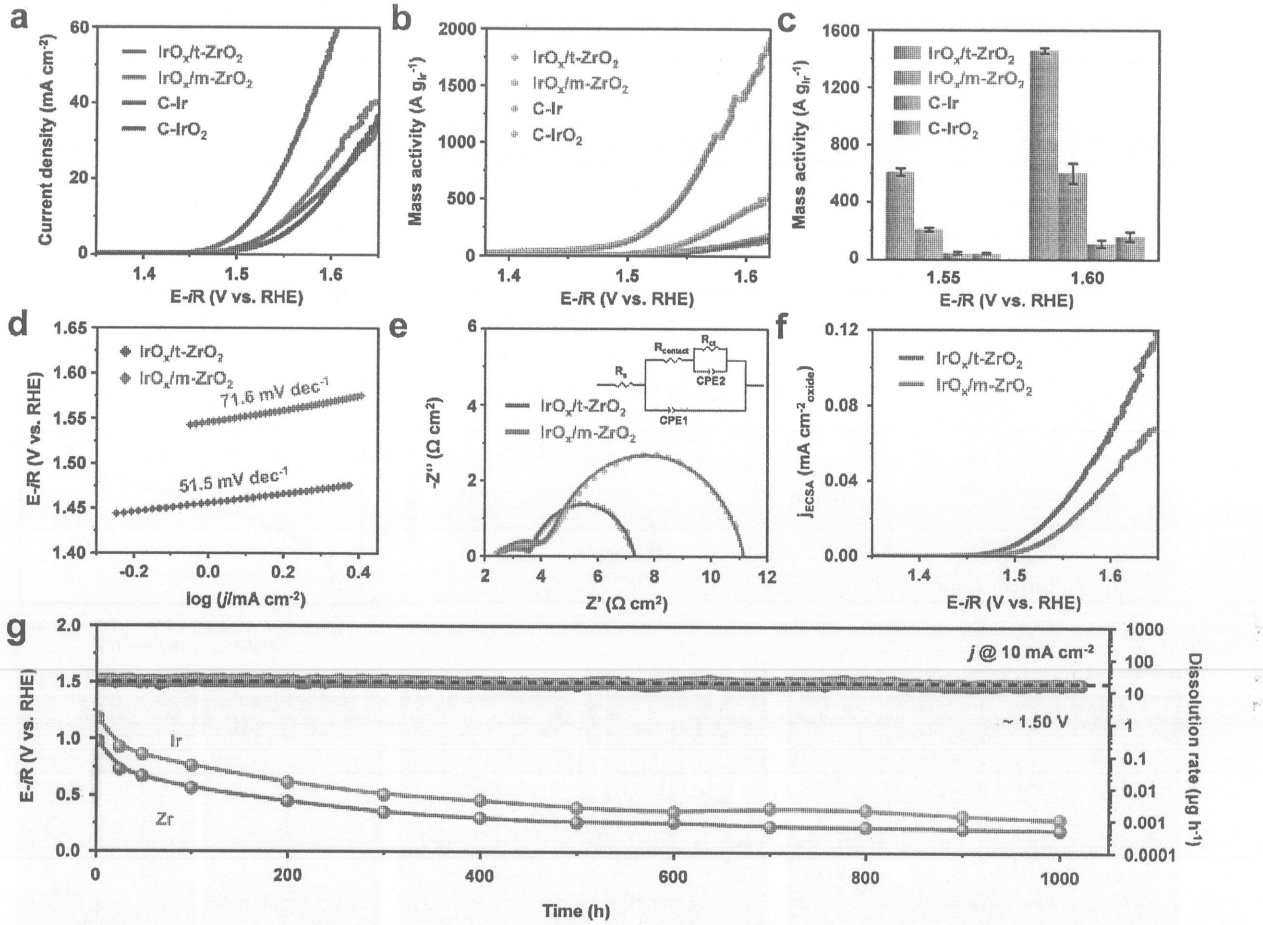

Fig. 3 OER performance evaluation in 0.1 M $HClO_4$ electrolyte. (a) LSV curves recorded at a scan rate of 5 mV s^{-1}, (b) corresponding mass activity and (c) specially activity calculated at 1.55 V and 1.60 V for IrO_x/t-ZrO_2 and control samples. (d) Tafel plots obtained from Fig. 3a. (e) EIS curve of IrO_x/t-ZrO_2 and IrO_x/m-ZrO_2 at 1.50 V *vs.* RHE. The inset in (e) illustrates the equivalent circuit diagram. (f) ECSA normalized current densities (j_{ECSA}). (g) Chronopotentiometric test at a constant current density of 10 mA cm^{-2} for more than 1000 h along with the time-dependent metal dissolution rate.

0.52% Ir loss and 0.09% of Zr loss after CP test (Table S1, ESI†). The stability number (S-number) was also evaluated as a description of electrocatalyst stability by calculating the oxygen evolved per Ir dissolved, and the S-number of IrO_x/t-ZrO_2 after 1000 h reaction was calculated as 3.6×10^6 n_{O_2} n_{Ir}^{-1}. It is noteworthy that the stability of IrO_x/t-ZrO_2 surpasses the majority of previously reported Ir based catalyst using a similar Ir loading amount (Table S2, ESI†). Additionally, it was observed that the crystal structure and morphology remained unchanged after stability testing by using XRD, TEM and the atomic-resolution aberration-corrected HAADF-STEM to analyze the catalyst after reaction (Fig. S16, S17a–e and S18a–d, ESI†). The particle sizes of IrO_x were also measured and found that there was only a slight change in the size of IrO_x particle sizes (from 1.34 nm to 1.38 nm) (Fig. S19a and b, ESI†). All of the above evidence demonstrated the excellent stability of the IrO_x/t-ZrO_2 catalyst for acidic water oxidation.

Identification of the LOM pathway for IrO_x/t-ZrO_2

To determine the effect of t-ZrO_2 on the electrochemical performance, we examined the OER mechanism of the catalysts. In the LOM or AEM pathway, oxidized oxygen (O^-) and superoxide (O_2^-) negative species will be generated, respectively, and tetramethylammonium (TMA^+) can coordinate with O^-, occupy the active sites and thus lead to a reduced OER catalytic current through LOM, which can be used as a chemical probe to monitor the LOM pathway.[22,45,46] As shown in Fig. S20a and b (ESI†), after adding TMA^+, a decreased activity could be observed in the LSV curves of both IrO_x/t-ZrO_2 and commercial RuO_2 (which follows a LOM pathway) indicating the participation of the LOM,[26] while the similar OER performance of IrO_x/m-ZrO_2 and commercial IrO_2 (following an AEM pathway) in Fig. S20c and d (ESI†) reveals that the IrO_x/m-ZrO_2 follows an AEM pathway during the OER process. Moreover, pH-dependency tests were also carried out,[22,23,25] and a clear distinction could be found between IrO_x/t-ZrO_2 and IrO_x/m-ZrO_2. For IrO_x/t-ZrO_2, a pH-dependent OER kinetics with a slope, which is close to the theoretical value of the LOM pathway, of approximately 60 mV dec^{-1}, was observed[47] (Fig. 4a and Fig. S21, ESI†). For IrO_x/m-ZrO_2, however, an opposite pH-independent OER kinetics can be observed (Fig. 4b and Fig. S22, ESI†), showing a typical AEM pathway.

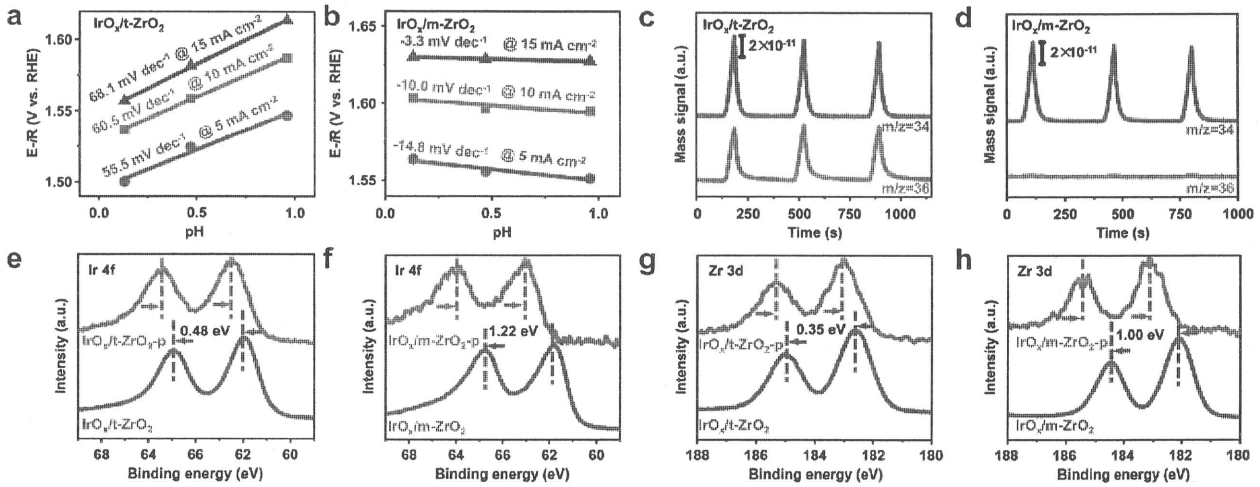

Fig. 4 Verification of the LOM pathway over IrO_x/t-ZrO_2 catalyst. (a) and (b) pH dependence on the OER potential at different current densities (5, 10 and 15 mA cm^{-2}) for (a) IrO_x/t-ZrO_2 and (b) IrO_x/m-ZrO_2. (c) and (d) DEMS tests of $^{18}O^{16}O$ and $^{18}O^{18}O$ signals from the ^{18}O-labeled (c) IrO_x/t-ZrO_2 and (d) IrO_x/m-ZrO_2 in 0.1 M $HClO_4$ in $H_2{}^{16}O$. (e) and (f) XPS spectra of Ir 4f of (e) IrO_x/t-ZrO_2 and IrO_x/t-ZrO_2 after reaction (10 h@10 mA cm^{-2} in 0.1 M $HClO_4$) and (f) IrO_x/m-ZrO_2 and IrO_x/m-ZrO_2 after reaction (10 h @ 10 mA cm^{-2} in 0.1 M $HClO_4$) (g, h) XPS spectra of Zr 3f of (g) IrO_x/t-ZrO_2 and IrO_x/t-ZrO_2 after reaction (10 h @ 10 mA cm^{-2} in 0.1 M $HClO_4$) and (h) IrO_x/m-ZrO_2 and IrO_x/m-ZrO_2 after reaction (10 h@10 mA cm^{-2} in 0.1 M $HClO_4$).

To further validate the existence of LOM, *in situ* ^{18}O-labeled differential electrochemical mass spectrometry was utilized.[22,25] IrO_x/t-ZrO_2 and IrO_x/m-ZrO_2 were firstly labeled by ^{18}O though pretreating in 0.1 M $HClO_4$ with $H_2{}^{18}O$ as solvent. Both ^{34}O ($^{18}O^{16}O$) and ^{36}O ($^{18}O^{18}O$) were detected during the OER process of IrO_x/t-ZrO_2 (Fig. 4c), and higher than the natural isotopic abundance of ^{18}O ($\leq$0.2%) in H_2O, indicating the LOM pathway.[25] In contrast, following the AEM pathway, no ^{36}O signals were detected during the OER process of IrO_x/m-ZrO_2 (Fig. 4d).

X-ray photoelectron spectroscopy (XPS) and X-ray absorption fine structure (XAFS) were further used to study the chemical state and coordination environment of the catalysts, providing insights into the tendencies of the OER pathways. The *ex situ* Ir 4f XPS spectra showed that only a 0.48 eV positive energy shift can be found after 10 h reaction at 10 mA cm^{-2} in IrO_x/t-ZrO_2 (Fig. 4e). For IrO_x/m-ZrO_2, however, a significant positive energy shift of 1.22 eV was discovered under the same conditions (Fig. 4f, which indicates the impact of the different OER pathway on the surface valence state, and the larger energy shift may be caused by the overoxidation of Ir sites in the AEM pathway. Similarly, for Zr of IrO_x/t-ZrO_2, the *ex situ* Zr 3d XPS also showed that IrO_x/t-ZrO_2 exhibited a lower positive energy shift (0.35 eV) (Fig. 4g) compared to that of IrO_x/m-ZrO_2 (1.00 eV) (Fig. 4h), which indicates a stronger interaction between the support and IrO_x in IrO_x/t-ZrO_2 with oxygen species migration from Zr sites to avoid its overoxidation.

The white line (WL) peak intensity of the Ir L_3-edge in the X-ray absorption near-edge structure (XANES) spectra (Fig. S23a, ESI†), represents the oxidation state of Ir, suggesting the lower valence state of Ir in IrO_x/t-ZrO_2 which can be ascribed to the metal oxide support interactions between IrO_x and t-ZrO_2. However, the IrO_x/t-ZrO_2 after the OER showed an increased valence state indicating an evolution of the chemical environment during the reaction. The Fourier transform extended X-ray absorption fine structure (FT-EXAFS) data also reveal the local Ir–O environment. As shown in Fig. S23b (ESI†), influenced by the considerable Ir–O–Zr interface, the Ir–O bond length in IrO_x/t-ZrO_2 (1.63 Å) was elongated, approximately 4.5% longer than the Ir–O bond length in IrO_2 (1.56 Å), indicating a weakening of the Ir–O bond. Additionally, the coordination number of Ir–O in IrO_x/t-ZrO_2 was much lower compared to IrO_2 indicating that the IrO_x cluster in IrO_x/t-ZrO_2 is very small and possesses abundant Ir–O–Zr interfaces. Similarly, for the XANES data, the IrO_x/t-ZrO_2 after the OER also showed a shrinkage of the Ir–O bond (1.58 Å) of approximately 3% compared to the origin states indicating the increased valence state. In other words, both the XPS and XANES data suggest that t-ZrO_2 provides a different chelation environment to Ir sites, and the accommodation of IrO_x clusters into the form leads to a higher surface chemical state which is preferred for LOM paths.[48] In contrast, for Zr only a slight difference in the electronic structure or local coordination environment could be observed from XANES spectra and FT-EXAFS data (Fig. S24a and b, ESI†), indicating that the low Ir loading amount could hardly influence the bulk structure of t-ZrO_2.

Evidence for the oxygen spillover stabilized LOM pathway

Previous *ex situ* XPS has demonstrated that both the Ir and Zr sites of IrO_x/t-ZrO_2 exhibited a lower binding energy shift compared to IrO_x/m-ZrO_2 after the OER process, indicating that the overoxidation of Ir was inhibited and the spillover of oxygen from Zr to Ir sites occurred. To further elucidate the counter-intuitive stability of the IrO_x/t-ZrO_2, *operando* XAFS analysis was conducted on a homemade cell (Fig. S25, ESI†) to reveal the local structural evolution during the OER process. Fig. 5a and b showed the *operando* Ir L_3-edge XANES spectra of the IrO_x/t-ZrO_2, recorded at different applied bias. Once the bias was

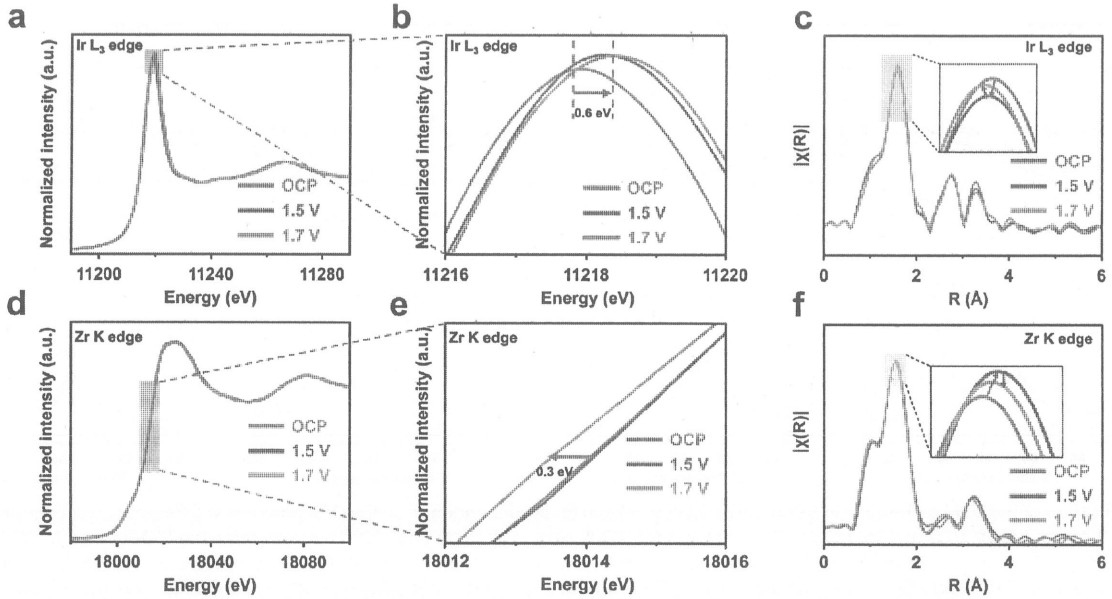

Fig. 5 Evidence for the oxygen spillover stabilized lattice oxygen mechanism pathway. (a) and (b) *Operando* Ir L_3-edge XANES spectra of IrO_x/t-ZrO_2 at different potentials in 0.1 M $HClO_4$. (b) is the enlargement of the white line peaks in (a). (c) *Operando* FT-EXAFS spectra of the Ir *R* space for IrO_x/t-ZrO_2. (d) and (e) *Operando* Zr K-edge XANES spectra of IrO_x/t-ZrO_2 at different potentials in 0.1 M $HClO_4$ (e) is the enlargement of the white line in (d). (f) *Operando* FT-EXAFS spectra of Zr *R* space for IrO_x/t-ZrO_2.

applied (from OCP to 1.5 V *vs.* RHE), the white-line peak intensified and shifted positively, showing a fast increase in the valence state of Ir. This is attributed to the electron transformation from Ir to oxygen species, which indicates the kinetic oxidation through the LOM pathway.[49] However, when the bias was further increased (from 1.5 to 1.7 V), to our surprise, the white-line peak remained nearly unchanged, which indicates that the Ir was stable in its valence state during the OER process. This finding demonstrates that the catalyst structure can avoid collapsing due to the formation of oxygen vacancies through the spillover of oxygen from the support to Ir sites.

The *operando* Ir L_3-edge FT-EXAFS spectra can also reflect the evolution of local structures. As shown in Fig. 5c, the first shell peak of the Ir–O bond can be found at approximately 1.60 Å. Compared to the initial state (OCP), the peak weakened (oxygen vacancy generation), while the bias (1.5 V) was applied and exhibited a slight shift in *R* from 1.60 to 1.57 Å. With the applied bias increasing to 1.7 V, however, the Ir–O coordination peak intensified slightly, with further shift in *R* from 1.57 to 1.56 Å. These results imply that at the beginning of the OER process, the coordination structure of Ir was rearranged to react *via* the LOM pathway. During the OER process, the oxygen vacancy can be filled promptly, thus avoiding possible structure collapse caused by oxygen vacancies, to stabilize the configurations of Ir sites. In contrast, when the applied bias was increased (from 1.5 to 1.7 V), the *operando* XANES spectra of the Zr K-edge showed an opposite tendency and shifted to a lower energy (−0.3 eV energy shift was detected), revealing a decrease in the Zr valence state and possible oxygen spillover from Zr sites to Ir sites (Fig. 5d and e). Additionally, the first shell peak of the Zr–O bond can also be found from Zr K-edge FT-EXAFS spectra (Fig. 5f) at approximately 1.55 Å. The first-shell peak also weakened during the OER process (from 1.5 to 1.7 V), which is in agreement with the XANES spectra and reflected that the coordination number of Zr–O decreased, suggesting the oxygen removal process.

Additionally, *operando* surface-enhanced infrared absorption spectroscopy (SEIRAS) was conducted to study the oxygen species during the OER procedure. As demonstrated in Fig. S26a (ESI†), with the applied bias increased (from 1.1 V *vs.* RHE to 1.6 V *vs.* RHE); for IrO_x/t-ZrO_2, three absorption peaks at 1054 cm^{-1}, 1128 cm^{-1} and 1140 cm^{-1} appeared. Among them, the absorption peaks at 1054 cm^{-1} and 1140 cm^{-1} related to the *OO reaction intermediate[35,50] indicate the process of the OER, while the absorption peak at 1128 cm^{-1} related to the *OO* reaction intermediate[51] indicating the LOM of IrO_x/t-ZrO_2 for the OER. In contrast, for IrO_x/m-ZrO_2 (Fig. S26b, ESI†), only two absorption peaks at 1055 cm^{-1} and 1145 cm^{-1} appeared, suggesting the AEM of IrO_x/t-ZrO_2 for the OER.

Moreover, *operando* Raman was further conducted to study the change of valence state of metal sites. As shown in Fig. S27 (ESI†), three peaks appearing at 446 cm^{-1} 577 cm^{-1} and 719 cm^{-1}, and the peak appearing at 577 cm^{-1} are related to Ir-μ-oxo stretches that involve an Ir^{3+} species, while the peaks appearing at 446 cm^{-1} and 719 cm^{-1} are associated with the Ir-μ-oxo stretches that involve an Ir^{4+} species.[52,53] With increasing the applied bias (from 1.1 V *vs.* RHE to 1.7 V *vs.* RHE), the intensity of the peaks remained unchanged, implying that due to the oxygen spillover-stabilized LOM pathway, the Ir species had not been oxidized to a higher valence state.

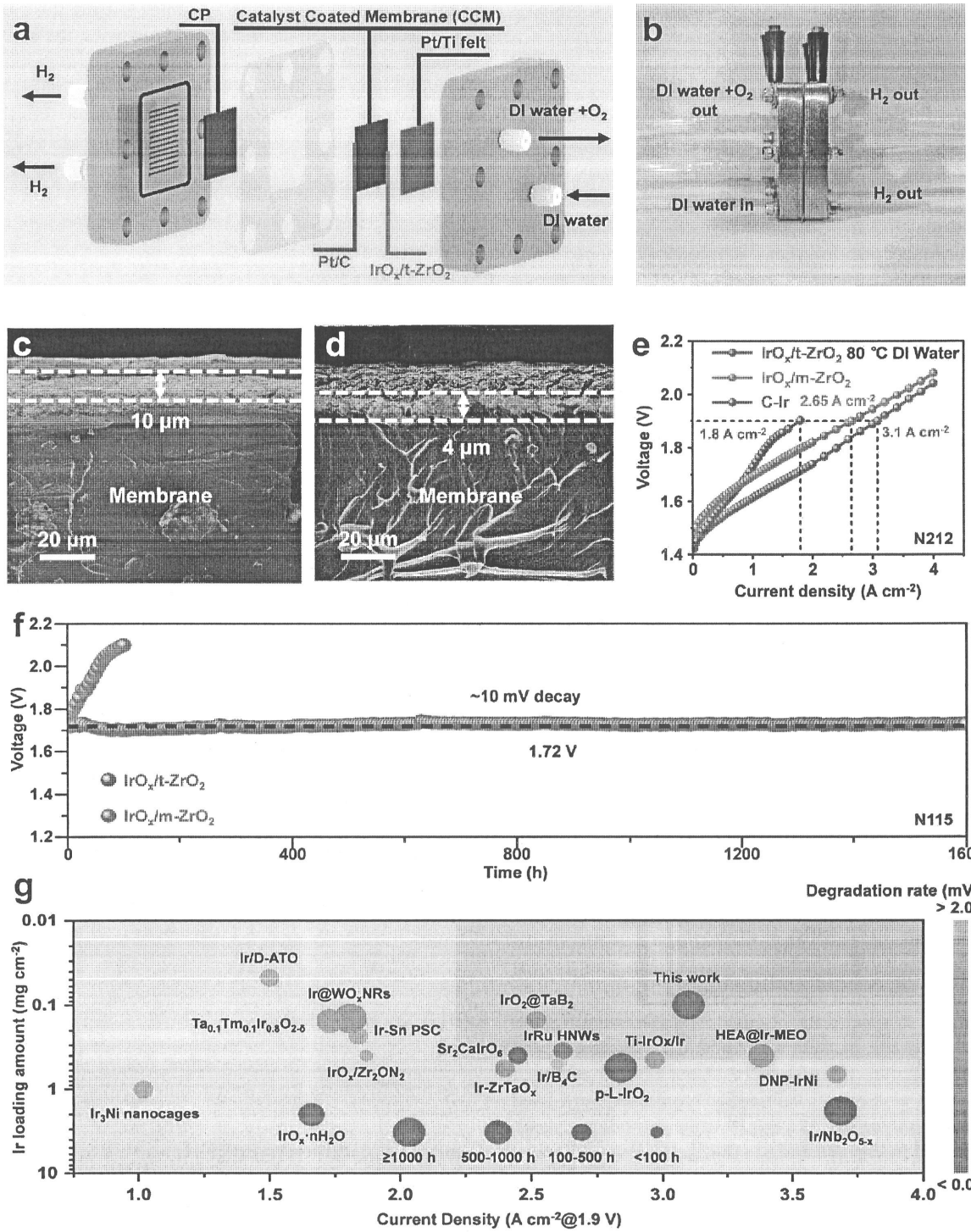

Fig. 6 PEM electrolysis performance using IrO_x/t-ZrO_2 as an anode electrocatalyst. (a) and (b) Schematic diagram and digital photograph of the PEM electrolyzer. (c) and (d) SEM image of the (c) IrO_x/t-ZrO_2 and (d) IrO_x/m-ZrO_2 anode layers in CCM with an anodic catalyst loading of 0.5 mg cm^{-2}. (e) Polarization curve of the PEM electrolyzer using IrO_x/t-ZrO_2 (0.5 mg cm^{-2}, 0.1 mg_{Ir} cm^{-2}), IrO_x/m-ZrO_2 (0.5 mg cm^{-2}, 0.12 mg_{Ir} cm^{-2}) and commercial Ir black (2 mg cm^{-2}, 2 mg_{Ir} cm^{-2}) as anodic catalysts and 40% Pt/C (1 mg cm^{-2}, 0.4 mg_{Pt} cm^{-2}) as cathodic catalyst obtained at 80 °C with a Nafion 212 membrane. (f) Chronopotentiometry curve of the PEM electrolyzer using IrO_x/t-ZrO_2 and IrO_x/m-ZrO_2 catalyst operated at 1 A cm^{-2} at 80 °C with the Nafion 115 membrane. (g) A comparison of Ir loading amount, current density at 1.9 V, degradation rate and operation time of IrO_x/t-ZrO_2 with reported anode catalyst in a PEM electrolyzer.

PEM water electrolysis performance using IrO_x/t-ZrO_2 anode catalysts

Finally, a PEM electrolyzer was assembled (Fig. 6a and b and Fig. S28, ESI†) with IrO_x/t-ZrO_2 as the anode catalyst to evaluate the benefits of oxygen spillover stabilized LOM. The PEM electrolyzer was customized using an anodic IrO_x/t-ZrO_2 catalyst loading of 0.5 mg cm^{-2} (0.1 mg_{Ir} cm^{-2}) and operated at 80 °C feeding with DI water. IrO_x/m-ZrO_2 with nearly the same amount of catalyst loading (0.5 mg cm^{-2}, 0.12 mg_{Ir} cm^{-2}) and a commercial PEM electrolyzer with 2 mg cm^{-2} of Ir black in the anode were prepared for direct comparison. Benefitting from the porous architecture, mass transport can be improved and a thicker anodic catalyst layer of IrO_x/t-ZrO_2 (10 μm) (Fig. 6c) can be achieved compared to the catalyst layer that composed of traditional nanoparticles (IrO_x/m-ZrO_2, 4 μm) (Fig. 6d) with the same mass loading of 0.5 mg cm^{-2}. The appropriate thickness can avoid poor electrical contact between the catalyst layer and the porous transport layer, which causes low Ir utilization when reducing the catalyst loading.[20] As shown in Fig. 6e, the polarization curve verified the boosted catalytic activity of IrO_x/t-ZrO_2, showing a current density of 3.10 A cm^{-2} at 1.9 V, outperforming IrO_x/t-ZrO_2 (2.65 A cm^{-2} at 1.9 V) and commercial Ir black (1.80 A cm^{-2} at 1.9 V). Moreover, IrO_x/t-ZrO_2 exhibits extraordinary mass activity (31000 A g_{Ir}^{-1}) and is 1.40 times and 34.4 times that of IrO_x/t-ZrO_2 (22083 A g_{Ir}^{-1}) and commercial Ir black (900 A g_{Ir}^{-1}) at 1.9 V, respectively. EIS experiments on PEM electrolyzers were also carried out to study the origin of different performances. As shown in Fig. S29 and Table S3 (ESI†), the EIS results fitted based on the equivalent circuit illustrated that the lowest ohmic resistance (118 mΩ cm^2) and charge transfer resistance (39.25 mΩ cm^2) were achieved due to the enhanced mass transfer and optimized interface contact of IrO_x/t-ZrO_2.

To assess long-term stability in a PEM electrolyzer, a CP test was conducted at a constant current of 1 A cm^{-2}. Impressively, only 6.25 μV h^{-1} activity decay can be observed during the 1600 h test, suggesting the robustness of the oxygen spillover stabilized LOM (Fig. 6f). In sharp contrast, the IrO_x/m-ZrO_2 lost its activity within the first 100 h of operation.

Additionally, to specifically eliminate interference originating from non-anodic catalyst sources and better isolate the intrinsic performance characteristics of our anodic catalysts, alternative PEM electrolyzer fabrication processes were used (typically, using 0.5 mg cm^{-2} 75% Pt/C as the cathodic catalyst). As demonstrated in Fig. S30 and S31 (ESI†), IrO_x/t-ZrO_2 showed a current density of 3.24 A cm^{-2} and 2.39 A cm^{-2} at 1.9 V with the Nafion 212 membrane and Nafion 115 membrane, respectively, outperforming the other control samples. CP tests at current densities of 1 A cm^{-2} and 2 A cm^{-2} are also obtained and as demonstrated in Fig. S32 and S33 (ESI†), negligible decays could be found after 150 h tests. Besides, the dissolution rate of Ir and Zr was also calculated from ICP-MS measurements after the stability tests at 1 A cm^{-2} and 2 A cm^{-2} for 150 hours (Fig. S34, ESI†). The results indicate 1% Ir loss and 0.01% Zr loss for IrO_x/t-ZrO_2 after 150 hours of working at 1 A cm^{-2}, and 1.65% Ir loss and 0.03% Zr loss for IrO_x/t-ZrO_2 after 150 hours of working at 2 A cm^{-2}. Despite the differences in the cathodic catalysts and membrane types, the comparison demonstrates the high performance and long-term stability of the oxygen spillover stabilized LOM of IrO_x/t-ZrO_2. Consequently, it could be found that our IrO_x/t-ZrO_2 catalyst outperforms most of the PEM electrolyzers using other reported advanced Ir-based catalysts in many aspects, such as stability, Ir loading amount and performance (Fig. 6g and Table S4, ESI†).

Conclusions

In summary, we have successfully developed a low-Ir loading anode electrocatalyst of IrO_x/t-ZrO_2 which mediates a robust lattice oxygen engaged acidic water oxidation. *Operando* X-ray characterization studies and theoretical calculations demonstrate an oxygen spillover stabilized LOM pathway, with oxygen migrating from t-ZrO_2 supports to IrO_x sites to fill the lost lattice oxygen in time and avoid soluble $*V_O$–IrO_4^{2-} intermediates. The resultant IrO_x/t-ZrO_2 enables a highly efficient and stable OER process in a PEM water electrolyzer, with an extremely low Ir loading of 0.1 mg_{Ir} cm^{-2}, which can continuously run for more than 1600 h at 1 A cm^{-2} with low activity decay (6.25 μV h^{-1}). This work not only inspires the subtle modulation of oxygen pathways between the active sites and supports for acidic water oxidation, but also offers a promising path to next-generation PEM electrolyzers with low Ir loading amount.

Author contributions

P. F. L. and H. G. Y. conceived and designed the research. H. Y. Y., P. F. L. and H. G. Y. supervised the research. S. R. F. carried out most of the experiments and wrote the first version of the manuscript. H. X. Y. and H. Y. Y. performed the calculations. H. Y. L., M. Y. L., F. X. M., H. Q. F., H. F. and C. S. helped part of the experiments. All authors discussed, read and commented on the manuscript.

Data availability

The data supporting this study's findings are available from the corresponding author upon reasonable request.

Conflicts of interest

The authors declare no competing interest.

Acknowledgements

This work was financially supported by the National Natural Science Foundation of China (22239001, 22379043 and 22472053), the Shanghai Pilot Program for Basic Research (22TQ1400100-12), the Science and Technology Commission of Shanghai Municipality (23520710700), and the Fundamental Research Funds for the Central Universities. The authors would like to thank

Shanghai Aitins Technology Co., Ltd. for their professional support and assistance in first-principles calculations. The authors also thank the Frontiers Science Center for Materiobiology and Dynamic Chemistry, and the 1W1B- XAFS Beamline of Beijing Synchrotron Radiation Facility (**https://cstr.cn/31109.02.BSRF.1W1B**) for providing technical support and assistance in XAFS data collection.

References

1 M. Carmo, D. L. Fritz, J. Mergel and D. Stolten, *Int. J. Hydrogen Energy*, 2013, **38**, 4901–4934.
2 L. C. Seitz, C. F. Dickens, K. Nishio, Y. Hikita, J. Montoya, A. Doyle, C. Kirk, A. Vojvodic, H. Y. Hwang, J. K. Norskov and T. F. Jaramillo, *Science*, 2016, **353**, 1011–1014.
3 A. Li, S. Kong, K. Adachi, H. Ooka, K. Fushimi, Q. Jiang, H. Ofuchi, S. Hamamoto, M. Oura, K. Higashi, T. Kaneko, T. Uruga, N. Kawamura, D. Hashizume and R. Nakamura, *Science*, 2024, **384**, 666–670.
4 H. B. Tao, H. Liu, K. Lao, Y. Pan, Y. Tao, L. Wen and N. Zheng, *Nat. Nanotechnol.*, 2024, **19**, 1074–1076.
5 B. Lu, C. Wahl, R. dos Reis, J. Edgington, X. K. Lu, R. Li, M. E. Sweers, B. Ruggiero, G. T. K. K. Gunasooriya, V. Dravid and L. C. Seitz, *Nat. Catal.*, 2024, **7**, 868–877.
6 M. A. Hubert, L. A. King and T. F. Jaramillo, *ACS Energy Lett.*, 2022, **7**, 17–23.
7 J. Xu, H. Jin, T. Lu, J. Li, Y. Liu, K. Davey, Y. Zheng and S. Z. Qiao, *Sci. Adv.*, 2023, **9**, eadh1718.
8 Z. P. Shi, J. Li, J. D. Jiang, Y. B. Wang, X. Wang, Y. Li, L. T. Yang, Y. Y. Chu, J. S. Bai, J. H. Yang, J. Ni, Y. Wang, L. J. Zhang, Z. Jiang, C. P. Liu, J. J. Ge and W. Xing, *Angew. Chem., Int. Ed.*, 2022, **61**, e202212341.
9 Z. Xie, X. Liang, Z. Kang, Y. Zou, X. Wang, Y. A. Wu, G. King, Q. Liu, Y. Huang, X. Zhao, H. Chen and X. Zou, *CCS Chem.*, 2025, **7**, 216–228.
10 S. Hao, H. Sheng, M. Liu, J. Huang, G. Zheng, F. Zhang, X. Liu, Z. Su, J. Hu, Y. Qian, L. Zhou, Y. He, B. Song, L. Lei, X. Zhang and S. Jin, *Nat. Nanotechnol.*, 2021, **16**, 1371–1377.
11 Z. Wang, Y.-R. Zheng, I. Chorkendorff and J. K. Nørskov, *ACS Energy Lett.*, 2020, **5**, 2905–2908.
12 M. Möckl, M. Bernt, J. Schröter and A. Jossen, *Int. J. Hydrogen Energy*, 2020, **45**, 1417–1428.
13 M. Möckl, M. F. Ernst, M. Kornherr, F. Allebrod, M. Bernt, J. Byrknes, C. Eickes, C. Gebauer, A. Moskovtseva and H. A. Gasteiger, *J. Electrochem. Soc.*, 2022, **169**, 064505.
14 X. Zheng, M. Qin, S. Ma, Y. Chen, H. Ning, R. Yang, S. Mao and Y. Wang, *Adv. Sci.*, 2022, **9**, 2104636.
15 S. Ge, R. Xie, B. Huang, Z. Zhang, H. Liu, X. Kang, S. Hu, S. Li, Y. Luo, Q. Yu, J. Wang, G. Chai, L. Guan, H.-M. Cheng and B. Liu, *Energy Environ. Sci.*, 2023, **16**, 3734–3742.
16 Y. Wang, M. Zhang, Z. Kang, L. Shi, Y. Shen, B. Tian, Y. Zou, H. Chen and X. Zou, *Nat. Commun.*, 2023, **14**, 5119.
17 C. Lee, K. Shin, Y. Park, Y. H. Yun, G. Doo, G. H. Jung, M. Kim, W. C. Cho, C. H. Kim, H. M. Lee, H. Y. Kim, S. Lee, G. Henkelman and H. S. Cho, *Adv. Funct. Mater.*, 2023, **33**, 2301557.
18 X. Han, T. Mou, A. Islam, S. Kang, Q. Chang, Z. Xie, X. Zhao, K. Sasaki, J. A. Rodriguez, P. Liu and J. G. Chen, *J. Am. Chem. Soc.*, 2024, **146**, 16499–16510.
19 G. Jiang, H. Yu, Y. Li, D. Yao, J. Chi, S. Sun and Z. Shao, *ACS Appl. Mater. Interfaces*, 2021, **13**, 15073–15082.
20 L. Tao, F. Lv, D. Wang, H. Luo, F. Lin, H. Gong, H. Mi, S. Wang, Q. Zhang, L. Gu, M. Luo and S. Guo, *Joule*, 2024, **8**, 450–460.
21 H. Zhong, Q. Zhang, J. Yu, X. Zhang, C. Wu, Y. Ma, H. An, H. Wang, J. Zhang, X. Wang and J. Xue, *Adv. Energy Mater.*, 2023, **13**, 2301391.
22 X. Wang, H. Zhong, S. Xi, W. S. V. Lee and J. Xue, *Adv. Mater.*, 2022, **34**, 2107956.
23 Z. Shi, Y. Wang, J. Li, X. Wang, Y. Wang, Y. Li, W. Xu, Z. Jiang, C. Liu, W. Xing and J. Ge, *Joule*, 2021, **5**, 2164–2176.
24 G. R. Lee, J. Kim, D. Hong, Y. J. Kim, H. Jang, H. J. Han, C. K. Hwang, D. Kim, J. Y. Kim and Y. S. Jung, *Nat. Commun.*, 2023, **14**, 5402.
25 A. Grimaud, O. Diaz-Morales, B. Han, W. T. Hong, Y.-L. Lee, L. Giordano, K. A. Stoerzinger, M. T. M. Koper and Y. Shao-Horn, *Nat. Chem.*, 2017, **9**, 457–465.
26 N. Yao, H. Jia, J. Zhu, Z. Shi, H. Cong, J. Ge and W. Luo, *Chem*, 2023, **9**, 1882–1896.
27 Z. Y. Wu, F. Y. Chen, B. Li, S. W. Yu, Y. Z. Finfrock, D. M. Meira, Q. Q. Yan, P. Zhu, M. X. Chen, T. W. Song, Z. Yin, H. W. Liang, S. Zhang, G. Wang and H. Wang, *Nat. Mater.*, 2023, **22**, 100–108.
28 Y. Wang, Z. Zhao, X. Liang, X. Zhao, X. Wang, S. Jana, Y. A. Wu, Y. Zou, L. Li, H. Chen and X. Zou, *Adv. Mater.*, 2024, **36**, 2407717.
29 W. He, X. Tan, Y. Guo, Y. Xiao, H. Cui and C. Wang, *Angew. Chem., Int. Ed.*, 2024, **63**, e202405798.
30 J. Cao, D. Zhang, B. Ren, P. Song and W. Xu, *Energy Environ. Sci.*, 2024, **17**, 5911–5921.
31 J. Chen, S. Xiong, H. Liu, J. Shi, J. Mi, H. Liu, Z. Gong, L. Oliviero, F. Mauge and J. Li, *Nat. Commun.*, 2023, **14**, 3477.
32 A. Parastaev, V. Muravev, E. Huertas Osta, A. J. F. van Hoof, T. F. Kimpel, N. Kosinov and E. J. M. Hensen, *Nat. Catal.*, 2020, **3**, 526–533.
33 V. Muravev, G. Spezzati, Y.-Q. Su, A. Parastaev, F.-K. Chiang, A. Longo, C. Escudero, N. Kosinov and E. J. M. Hensen, *Nat. Catal.*, 2021, **4**, 469–478.
34 G. N. Vayssilov, Y. Lykhach, A. Migani, T. Staudt, G. P. Petrova, N. Tsud, T. Skala, A. Bruix, F. Illas, K. C. Prince, V. Matolin, K. M. Neyman and J. Libuda, *Nat. Mater.*, 2011, **10**, 310–315.
35 W. Gou, S. Zhang, Y. Wang, X. Tan, L. Liao, Z. Qi, M. Xie, Y. Ma, Y. Su and Y. Qu, *Energy Environ. Sci.*, 2024, **17**, 6755–6765.
36 R. Huang, Y. Wen, P. Miao, W. Shi, W. Niu, K. Sun, Y. Li, Y. Ji and B. Zhang, *Chem Catal.*, 2023, **3**, 100667.
37 K. Rambabu, G. Bharath, A. F. Arangadi, S. Velu, F. Banat and P. L. Show, *Int. J. Hydrogen Energy*, 2020, **45**, 29668–29680.
38 J. E. Kim, Y. H. Yun, H. Park, J. Albers, G. Doo, S. Lee, J. Seo, C. Lee, M. Kim, H.-S. Cho, S.-K. Kim, J. H. Lee, Y.-W. Choi and J. H. Kim, *Fuel*, 2024, **376**, 132684.

39 H. Jin, S. Choi, G. J. Bang, T. Kwon, H. S. Kim, S. J. Lee, Y. Hong, D. W. Lee, H. S. Park, H. Baik, Y. Jung, S. J. Yoo and K. Lee, *Energy Environ. Sci.*, 2022, **15**, 1119–1130.
40 Y. Wen, C. Liu, R. Huang, H. Zhang, X. Li, F. P. Garcia de Arquer, Z. Liu, Y. Li and B. Zhang, *Nat. Commun.*, 2022, **13**, 4871.
41 X. Wang, H. Jang, S. Liu, Z. Li, X. Zhao, Y. Chen, M. G. Kim, Q. Qin and X. Liu, *Adv. Energy Mater.*, 2023, **13**, 2301673.
42 H.-Y. T. Chen, S. Tosoni and G. Pacchioni, *J. Phys. Chem. C*, 2014, **119**, 10856–10868.
43 S. Tosoni, H.-Y. T. Chen and G. Pacchioni, *Surf. Sci.*, 2016, **646**, 230–238.
44 A. R. C. Bredar, A. L. Chown, A. R. Burton and B. H. Farnum, *ACS Appl. Energy Mater.*, 2020, **3**, 66–98.
45 L. An, C. Wei, M. Lu, H. Liu, Y. Chen, G. G. Scherer, A. C. Fisher, P. Xi, Z. J. Xu and C. H. Yan, *Adv. Mater.*, 2021, **33**, 2006328.
46 M. Zhang, M. de Respinis and H. Frei, *Nat. Chem.*, 2014, **6**, 362–367.
47 M. T. M. Koper, *Chem. Sci.*, 2013, **4**, 2710–2723.
48 Z. Shi, X. Wang, J. Ge, C. Liu and W. Xing, *Nanoscale*, 2020, **12**, 13249–13275.
49 H. Su, C. Yang, M. Liu, X. Zhang, W. Zhou, Y. Zhang, K. Zheng, S. Lian and Q. Liu, *Nat. Commun.*, 2024, **15**, 95.
50 M. Zhang, M. de Respinis and H. Frei, *Nat. Chem.*, 2014, **6**, 362–367.
51 C. Lin, J.-L. Li, X. Li, S. Yang, W. Luo, Y. Zhang, S.-H. Kim, D.-H. Kim, S. S. Shinde, Y.-F. Li, Z.-P. Liu, Z. Jiang and J.-H. Lee, *Nat. Catal.*, 2021, **4**, 1012–1023.
52 Z. Pavlovic, C. Ranjan, Q. Gao, M. van Gastel and R. Schlögl, *ACS Catal.*, 2016, **6**, 8098–8105.
53 Z. Pavlovic, C. Ranjan, M. van Gastel and R. Schlögl, *Chem. Commun.*, 2017, **53**, 12414–12417.